Contents lists available at ScienceDirect

Applied Catalysis B: Environmental

Effect of Mn substitution on the promoted formaldehyde oxidation over spinel ferrite: Catalyst characterization, performance and reaction mechanism

Peng Liu [a,c,d], Hongping He [a,d], Gaoling Wei [b], Xiaoliang Liang [a,d,*], Feihong Qi [a,d], Fuding Tan [a,c,d], Wei Tan [a,c,d], Jianxi Zhu [a,d], Runliang Zhu [a,d]

[a] CAS Key Laboratory of Mineralogy and Metallogeny, Guangzhou Institute of Geochemistry, Chinese Academy of Sciences, Guangzhou 510640, PR China
[b] Guangdong Institute of Eco-Environmental and Soil Sciences, Guangzhou 510650, PR China
[c] University of Chinese Academy of Sciences, Beijing 100049, PR China
[d] Guangdong Provincial Key Laboratory of Mineral Physics and Materials, Guangzhou 510640, PR China

ARTICLE INFO

ABSTRACT

The work reports the synthesis and characterization of manganese substituted spinel ferrites, and their application as catalysts for formaldehyde oxidation. Structure and cationic coordination environment of the prepared catalysts were investigated by XRD, Raman, XPS spectroscopy and TG-DSC analysis. Temperature-programmed reduction (TPR) was used to measure the reducibility of catalysts. The characterization results reveal the formation of spinel structure in all the synthetic catalysts. The Mn cations enrich on the surface in the valence of +3 and +4. Mn substitution obviously increases the lattice oxygen content, facilitates the reduction of ferrite, and enhances the oxidative ability of Fe^{3+} and Mn cations on the catalyst surface. The presence of Mn cations in spinel ferrite greatly improves its catalytic activity in formaldehyde oxidation, evidenced by the obvious decrease of 90% formaldehyde conversion temperature. The studied catalyst also displays high stability and superior activity in the presence of water vapor, which presents an applied interest. The remarkable effect of Mn substitution on the promoted formaldehyde oxidation over spinel ferrite catalysts was discussed in view of reaction mechanism and variations in microstructural environment and physicochemical properties of spinel ferrite.

© 2015 Elsevier B.V. All rights reserved.

1. Introduction

As one of the toxic volatile organic compounds (VOCs), formaldehyde (HCHO) has been classified as a human carcinogen that causes nasopharyngeal cancer and probably leukemia [1]. With high consumption in the industrial processes such as the manufacturing of wood products and building materials, petrochemical engineering and combustion processes [2,3], its emission has become a great threat to the environment and human health [4]. Therefore, the abatement of HCHO before emission is highly desirable, and several techniques, e.g., adsorption [5], condensation [6], photo-catalysis [7] and catalytic oxidation [8], have been developed.

Among the various techniques for HCHO removal, catalytic oxidation is considered as the most ideal way, from the economical point of view, due to its low operation temperature (200–500 °C), highly destructive efficiency, and no additional fuel or harmful by-products [9]. To improve the performance of catalyst, much attention has been paid to its catalytic activity at low temperature. From previous studies, effective catalysts include the supported precious metals [10–12] and transition metal oxides [13,14]. By comparison, precious metals (e.g., Pt, Pd, etc.) loaded on the oxides and clays exhibit higher activity at relatively low temperature, but their high cost, easily sintering, and susceptibly poisoning prevent their application [15,16]. Transition metal oxides (e.g., Fe_2O_3, Cr_2O_3, CuO, NiO, Co_3O_4 and MnO_2) with fast electron transfer and variable valences have been the alternatives to precious metals, for their merits, such as low cost, high resistance to sulfur and chlorine, and good reducibility [17–19]. The combination of two or more transition metal oxides displays higher catalytic activity than single metal oxide [20], even equivalent or better than precious metals because of the synergistic effects. The composite oxides such

as Mn–Cu–O [20], Co–Ce–O [21] and Co–Mn–O [9] have showed promising performance in the catalytic oxidation of HCHO.

Binary spinel-type oxides represent a key group of catalysts for HCHO oxidation, and exhibit generally better activity than the simple mixture of the corresponding single oxides [22]. The formula of spinel can be written as AB_2O_4, where A and B denote divalent and trivalent metal cations, respectively. In the normal structure, A cations occupy 8 of 64 available tetrahedral sites, while B cations occupy 16 of 32 available octahedral sites. In the inverse structure, all the A cations and one-half of the B cations have exchanged site occupancy. The high lattice-defect density [23] and surface coverage of −OH groups or oxygen ions [24] endow spinel oxides strong catalytic activity. In the last few years, spinel ferrites have been extensively pursued, due to their high thermal resistance, strong magnetism and catalytic activity [25]. The substitution of transition metals (Co, Ni, Cu, Zn) in spinel ferrites has been found modifying its redox activity of ferrites [26–30]. The transition metal dopants in the spinel structure generally promote the formation of mixed or inverse spinel structures [31]. The physico-chemical properties of ferrites are strongly dependent on the sites, nature and amount of the transition metals on the octahedral or tetrahedral sites in the spinel structure [27]. In most instances, these substitutions improve the thermal, textural stability and redox properties. Moreover, the replacement of Fe^{3+} with other metals on the octahedral sites can affect the binding strength of metal–oxygen, resulting in different adsorption energies for −OH species at the catalytic sites [32].

Manganese oxides are promising, inexpensive, and nontoxic materials in environmental catalysis. Manganese with electronic structure $3d^5 4s^2$ has variable oxidation states from −3 to +7. Manganese oxides are capable of mobilizing electrons, and thus, of generating the mobile-electron environment required by catalysis. In terms of HCHO oxidation, manganese oxides with different valences [33], structures [34], morphology [35], and matrixes [36] have been widely used as catalysts and shown exciting performance. It is reported that MnO_x have been demonstrated to be more promising than some transition metal oxides, such as TiO_2, CoO, CeO_2, or some binary oxides for HCHO oxidation [35]. Manganese is also highly active component in spinel oxide catalysts, e.g., $Mn_xCu_yO_4$ [37], $Mn_xCo_yO_4$ [14], and $Mn_xMg_yO_4$ [38], for VOCs oxidation. The $Fe_xMn_yO_4$ spinel has been studied, where Mn in the spinel lattice can strongly influence their stability and modify the redox properties [39–41]. But to the best of our knowledge, this spinel oxide has been seldom tried in catalyzing the oxidation of VOCs, especially HCHO.

Hence, in this study, a series of Mn doped ferrites were used to catalyze HCHO oxidation, with emphasis on three aspects: (i) effect of Mn substitution on the catalytic performance and their application potential; (ii) the structural and physicochemical properties; (iii) the catalytic mechanism for HCHO oxidation. The aim of this work is to gain more insight into the relationship among the structural characters, physicochemical properties, and catalytic activity of Mn doped spinel ferrites, and develop this promising catalyst for HCHO oxidation.

2. Material and methods

2.1. Ferrite catalyst preparation

All chemicals and reagents used in this work were of analytical grade and used as received. The precursor of Mn substituted spinel ferrite, $Fe_{3-x}Mn_xO_4$, was prepared by the coprecipitation method. Firstly, $FeCl_3 \cdot 6H_2O$, $FeSO_4 \cdot 7H_2O$ and $MnSO_4 \cdot H_2O$ were dissolved in 400 mL of distilled water with $Fe^{3+}:Fe^{2+}:Mn^{2+}$ concentration ratio equal to 2:1 − x:x (total cation concentration = 0.75 mol L^{-1}),

where the value of x was set as 0, 0.2, 0.5 and 1.0. The pH was low enough (<1) to prevent iron oxidation and hydroxide precipitation. The above solution was added dropwise to a 210 mL solution of 4.0 mol L^{-1} NaOH under vigorous stirring at 25 °C. Then the mixed solution was further aged at 90 °C for 24 h. Quite low concentration of Fe and Mn cations was detected in the supernatant. It was necessary to emphasize that during the reaction, N_2 was passed through to prevent the oxidation of ferrous cation by air. After that, the precipitate was collected with centrifugation at 3500 rpm for 5 min, and washed by deionized water until neither Cl^- or SO_4^{2-} was detected. Finally, the precursor was dried in freezer drier and calcined in muffle furnace at 450 °C for 4 h to obtain the Mn substituted spinel ferrite. The prepared ferrite catalysts were labeled as Mn_x (x = 0, 0.2, 0.5 and 1.0).

A reference sample containing 12 wt.% Mn supported on Fe_2O_3 was synthesized by aqueous impregnation method [42], and labeled as 12% Mn/Fe_2O_3. Its activity was tested and compared to that of Mn0.5 with close Mn content, to illustrate the effect of structural Mn and Fe cations on the catalytic activity of ferrite. The preparation procedure is provided in text S1.

2.2. Ferrite catalyst characterization

The contents of Fe and Mn in the spinel ferrites were determined by PerkinElmer (PE) AAnalyst 400 Flame Atomic Absorption Spectrometry. Specific surface area measurements were carried out by using the BET method on the basis of the N_2 physisorption capacity at 77 K on an Micromeritics ASAP 2020 instrument. All the samples were degassed at 433 K for 12 h before test.

Powder X-ray diffraction patterns (PXRD) were recorded between 10° and 80° (2θ) at a step of 1° min^{-1} using a Bruker D8 advance diffractometer with Cu Kα radiation (40 kV and 40 mA). The crystallite size Dhkl was calculated by Scherrer equation. The reported crystallite sizes were determined by taking the average of the sizes at the peaks D220, D311, D400, D422, D511 and D440.

Raman spectra in the range of 150–1000 cm^{-1} were obtained on a RM2000 laser Raman spectrometer by employing 532 nm line of Ar ion laser. The reproducibility of peaks was adjusted by a silicon piece to 520 cm^{-1} before examination. The laser power and acquisition time were carefully controlled to avoid laser-induced thermal effect and oxidation.

Thermogravimetric and differential scanning calorimetry (TG-DSC) analyses were synchronously performed on a Netzsch STA 409 PC Instrument. About 20 mg of finely ground sample was heated in a corundum crucible from 30 to 1000 °C at a heating rate of 10 °C min^{-1} under dry air atomosphere (60 cm^3 min^{-1} at normal temperature and pressure).

X-ray photoelectron spectroscopy (XPS) analyses were performed using a Thermo Scientific K-Alpha instrument equipped with an Al Kα source (10 mA, 14 kV) and operating at 1486.8 eV during the measurement. The pass energy was set to 30 eV for high resolution analysis. Charge shift was corrected by adjusting the binding energy C 1s to 284.8 eV. The peak-fit processing was used with XPSPEAK program at a Lorentzian/Gaussian ratio of 80% after the substraction of Shirley-type background.

Temperature-programmed reduction (TPR) measurements were carried out using a quartz tube reactor with mass spectrometry (Hiden QIC-20) as a detector of H_2. About 100 mg sample was reduced by 10% H_2/Ar at the total flow rate of 100 mL min^{-1}. The temperature was in the range of 30–800 °C at a rate of 10 °C min^{-1}.

2.3. Formaldehyde oxidation catalyzed by spinel ferrites

The periodic steady-state activity of Mn substituted spinel ferrites for HCHO oxidation was tested in a fixed-bed reactor under

atmospheric pressure within temperature range of 100–400 °C (Eq. (1)).

$$HCHO + O_2 \rightarrow CO_2 + H_2O \tag{1}$$

The catalyst particles (100.0 mg and with particle size of 0.25–0.50 mm) were sandwiched in tubular fixed bed flow reactor of quartz (i.d. = 6 mm). The reactor was placed into a pipe furnace with the air hearting. The temperature was controlled with the accuracy ±0.5 °C using a temperature controller. The temperature was raised by 10 °C min^{-1} and stayed for 30 min at certain temperatures to achieve the steady state. The feed gas was 0.15 ± 0.01 vol.% HCHO balanced with the air (1500 ± 100 mL m^{-3}). The high concentration of HCHO used in this study was to simulate the removal of industrial formaledehyde [43–45]. Gaseous HCHO was generated by flowing dry air over the paraformaldehyde heated at 50 °C. Before feeding HCHO to the reactor, water was preliminary blown off from paraformaldehyde. The HCHO stream was then diluted by another dry air stream in the mixed gas cylinder to generate mixed gas. All the dry air was purified by sodium hydroxide particles to remove residual CO$_2$ and H$_2$O. In the water resistance experiment, the water was dosed in the gas mixture by the saturation of air stream at a given temperature. The total flow rate was 100 mL min^{-1}. Outlet gas from the reactor was quantified by the acetylacetone spectrophotometry method according to China national standard (GB/T15516-1995). The HCHO in the outlet gas was absorbed by the distilled water, then reacted with acetylacetone at pH 6 under boiling water bath, and completely converted to a stable yellow compound, 3,5-diacetyl-1,4-dityro-2,6-lutidine. The concentration of the stable yellow compound was analyzed by UV–vis spectrophotometer PE Lambda 850 at a wavelength of 413 nm, which was used to calibrate the HCHO concentration. The HCHO conversion rate was characterized by the following equation (Eq. (2)):

$$HCHO \text{ conversion rate} = \frac{1 - C_{HCHO}}{C_{*HCHO}} \times 100\% \tag{2}$$

where C$_{*HCHO}$ is the inlet concentration of HCHO and C$_{HCHO}$ is the outlet concentration at different temperatures.

The HCHO oxidation also was characterized by CO$_2$ generation rate (Eq. (3)):

$$CO_2 \text{ generation rate} = \frac{C_{CO2}}{C_{*CO2}} \times 100\% \tag{3}$$

where C$_{*CO2}$ is the concentration of CO$_2$ in the effluent when HCHO is oxidized completely and C$_{CO2}$ is that at different temperatures. The concentration of CO$_2$ in effluent was recorded by gas chromatography (GC, Agilent 7890A) equipped with thermal conductivity detector (TCD) detector. The GC oven was held at 70 °C for 5 min, temperature programmed to 130 °C at 15 °C min^{-1}, then to 180 °C at 25 °C min^{-1} and held at 180 °C for 4 min.

Recycle experiment was carried out to check the stability of catalyst. After the HCHO oxidation finished at 400 °C, the catalyst was left in the reactor and the heating was suspended. When reactor was cool down to room temperature under air atmosphere, another oxidation cycle was started by repeating the same oxidation procedure. The recycle experiment was carried out for three cycles.

3. Results and discussion

3.1. Chemical analysis and XRD characterization

The chemical compositions (Table 1) of the Mn substituted ferrites obtained from chemical analysis show that the increase of manganese content is followed by a simultaneous decrease of Fe content, while the oxygen content does not vary obviously. For all the samples, the Mn:Fe molar ratios are close to the theoretical

value, indicating the complete precipitation of Mn and Fe cations during the preparation of magnetite precursors.

Fig. 1a shows the PXRD patterns of as-prepared precursors along with the pattern of magnetite (JCPDS: 19-0629). All the precursors exhibit intense and similar types of PXRD patterns. The well resolved peaks clearly indicate the polycrystalline and monophasic nature of magnetite. Interestingly, with the increase of Mn content, both the intensity and sharpness of reflections increase, and the strong PXRD peak (3 1 1) at 35.5° gradually shifts to low angle. This suggests the incorporation of Mn in the spinel structure.

After the calcination in air at 450 °C, the obtained spinel ferrite phase detected by PXRD is given in Fig. 1b. Additional reflections related to the crystalline manganese oxides including Mn$_2$O$_3$ or MnO$_2$, are not present. Nevertheless, the identification of magnetite and maghemite phases by PXRD is quite intricate, because both phases pose the similar spinel structure and almost identical lattice parameter (a_0). But compared with magnetite, the diffraction reflections of maghemite (JCPDS:39-1346) appear at higher angle (Fig. 1a). a_0 of maghemite (0.8351 nm) is lower than that of magnetite (0.8396 nm), due to the smaller radius of Fe^{3+} (0.64 Å) than that of Fe^{2+} (0.78 Å). The XRD patterns of spinel ferrite samples correspond well to maghemite rather than magnetite (Fig. 1b), indicating the oxidation of magnetite precursor to maghemite (Eq. (4)). The (3 1 1) peak also shifts to low angle with the Mn substitution increase. With the exception of Mn1.0 sample, the presence of Mn enhances the intensity and sharpness of reflection peaks, suggesting the improvement effect of Mn cation with low content on the crystallization of spinel structure. For Mn1.0, the split of reflection peaks at high angle emerges, which may imply the mixture of different spinel phases or the changes in the cation ordering in the spinel structure.
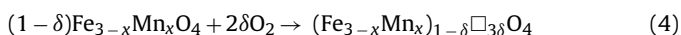
$$(1 - \delta)Fe_{3-x}Mn_xO_4 + 2\delta O_2 \rightarrow (Fe_{3-x}Mn_x)_{1-\delta}\square_{3\delta}O_4 \tag{4}$$

Table 1 also displays the a_0, crystal size and specific surface area of ferrite catalysts. With the increase of Mn substitution in the spinel ferrites, the a_0 obviously increases, ascribed to the larger radius of Mn^{3+} (0.72 Å) and Mn^{4+} (0.67 Å) than that of Fe^{3+} (0.64 Å) [46]. The a_0 variation indicates that Mn cations are incorporated into the spinel structure. Moreover, Mn incorporation greatly decreases the specific surface area of ferrites, while the crystal size locates in the range of 6.6–19.3 nm without obvious variation. A test with the magnet shows that all the prepared samples are magnetic and completely attracted to the magnet, which is helpful for their practical application with facile recycle.
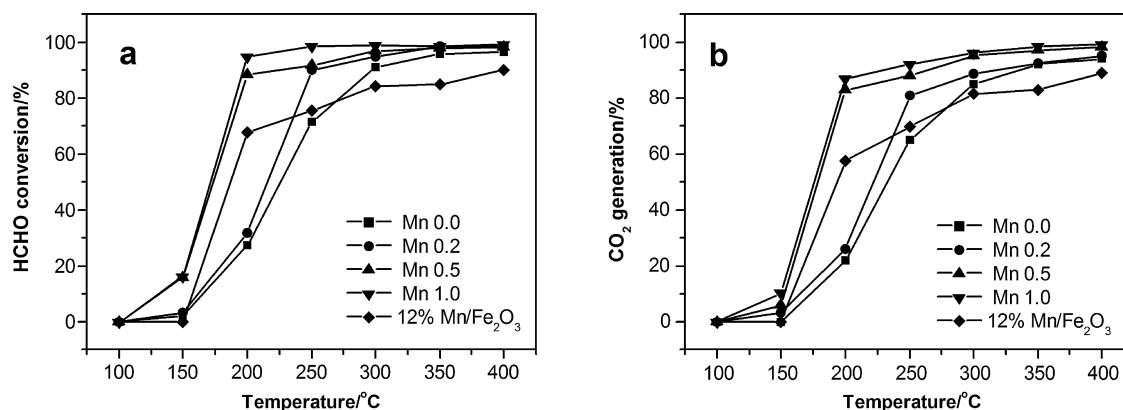
3.2. Catalytic activity for HCHO oxidation

The activity of Mn doped spinel ferrites for HCHO oxidation is shown by the conversion curves as a function of temperature, 100–400 °C (Fig. 2a). In order to check whether some reactions under thermal combustion condition could take place, blank test was carried out on non-coated mesh in the reactor, where low conversion (<10%) was observed below 400 °C. The temperatures of 10% (T10), 50% (T50), and 90% (T90) HCHO conversion over spinel ferrite catalysts are summarized in Table 2. The Mn0 sample without Mn substitution exhibited a considerable activity with T50 and T90 of 225 and 297 °C, respectively. With Mn incorporation, the catalytic performance of spinel ferrites was remarkably improved, and the conversion curves gradually shifted to low temperature. Interestingly, as evidenced by the variation of T50 and T90, the improvement of catalytic activity was obvious at low Mn substitution Mn/Fe = 0.2 (Mn0.5). However, with the increase of Mn content up to Mn/Fe = 0.2 (Mn0.5) or higher, the catalytic ability did not change distinctly, especially at low HCHO conversion rate. For example, the T50 by Mn0.5 (174 °C) was almost the same to that by Mn1.0 (171 °C). The main difference appears at high HCHO con-

Table 1
Chemical composition and main physico-chemical properties for Mn substituted spinel ferrite catalysts.

Samples	CMn (wt%)	CFe (wt%)	C_O (wt%)	Mn/Fe (mole)	Lattice parameter a_0 (Å)	Crystal size (nm)	Specific surface area ($m^2 g^{-1}$)
Mn0	0	65.9	34.1	0	8.354	6.6	73.6
Mn0.2	3.9	63.2	32.9	0.063	8.385	12.6	75.4
Mn0.5	12.0	56.9	31.1	0.22	8.393	19.3	60.7
Mn1.0	24.1	47.0	28.9	0.52	8.410	11.4	48.3
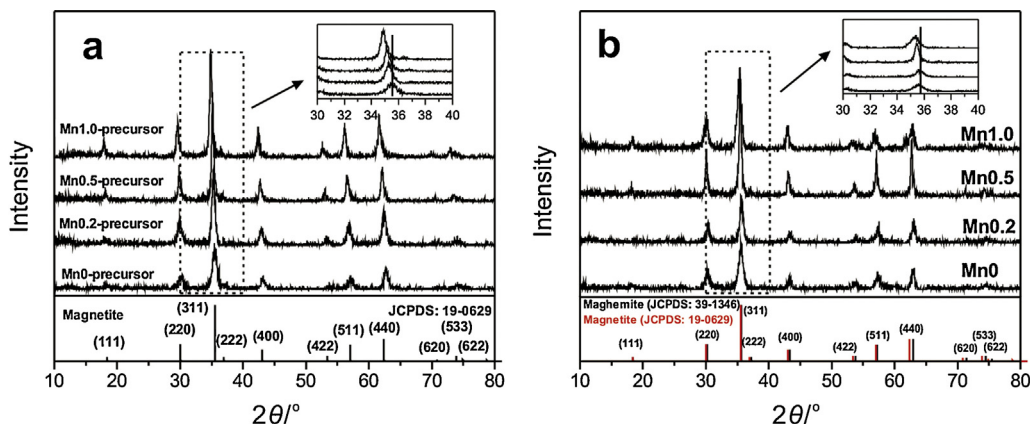
Fig. 1. The XRD patterns of precursors (a), Mn substituted spinel ferrites (b), and the standard card of magnetite (JCPDS:19-0629) and maghemite (JCPDS:39-1346).

Fig. 2. The conversion curves of HCHO oxidation and CO_2 generation over Mn substituted spinel ferrite.

Table 2
Catalytic activity of Mn substituted spinel ferrites for HCHO oxidation and CO_2 generation.

Samples	HCHO conversion temperature			CO_2 generation temperature		
	T10	T50	T90	T10	T50	T90
Mn0	165	225	297	173	233	336
Mn0.2	161	214	246	165	222	317
Mn0.5	131	174	228	151	178	266
Mn1.0	126	171	199	148	175	231
12%Mn–Fe2O3	157	186	398	159	193	398

version temperature, the T90 (199 °C) for Mn1.0 was higher than that of Mn0.5 (228 °C).

The CO_2 generation during the HCHO oxidation was also traced (Fig. 2b). The temperatures of 10% (T10), 50% (T50), and 90% (T90) CO_2 generation are displayed in Table 2. With the increase of Mn substitution, the CO_2 generation curves gradually shifted to low temperature, indicating the enhancement of catalytic activity of spinel ferrites. As seen from the variation of T10, T50, and T90 for CO_2 generation, they decreased obviously for the catalyst with low Mn substitution Mn/Fe = 0.2 (Mn0.5), but did not decrease greatly

for the catalyst with Mn content up to Mn/Fe = 0.2 (Mn0.5) or higher, except for the T90. The observations from CO_2 generation were identical to those from HCHO conversion.

However, compared to the HCHO conversion temperature, CO_2 generation temperature was not the same, but appeared at higher temperature. This indicated that HCHO was not completely oxidized to CO_2 and H_2O. From previous study, the byproducts in HCHO oxidation include HCOOH, CO and HCOOCH3 [47]. At low reaction temperature, the CO_2 generation rate was a bit lower than HCHO conversion rate. For example, for Mn0, Mn0.2, Mn0.5 and Mn1.0, the CO_2 generation rate at 200 °C was 22%, 26%, 83% and 87%, respectively, slightly lower than the HCHO conversion rate of 27%, 32%, 88% and 95%. But at high reaction temperature, for all the ferrite catalysts, the CO_2 generation rate became close to HCHO conversion rate (Fig. 2). This indicates the high selectivity to CO_2 for all the Mn substituted ferrite catalysts.

The supported sample labeled as 12% Mn/Fe2O3 was also tested for HCHO oxidation (Fig. 2). Although the reference sample contains similar Mn content to Mn0.5 (Table 1), its catalytic activity was much worse than that of Mn0.5. For example, T10, T50 and T90 in HCHO conversion by supported sample was 157, 186 and 398 °C, respectively, obviously higher than those by Mn0.5 (Table 2). More-
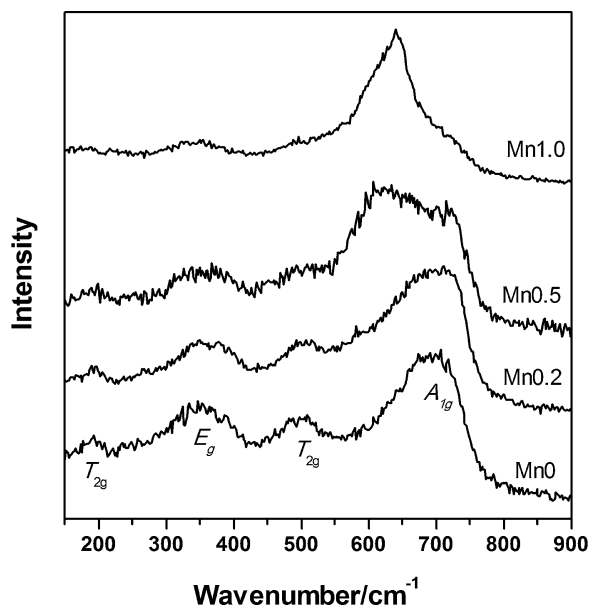
Fig. 3. Raman spectra of Mn-doped spinel ferrites.

Fig. 4. The TG-DSC curves of spinel ferrite precursors under air.

over, the CO_2 generation temperature by reference sample was also higher than Mn0.5 (Table 2). Thus, the activity of supported sample was worse than those of substituted sample with close Mn content. This indicates the important effect of structural Mn and Fe cations on the catalytic activity of ferrite.

To illustrate the improvement mechanism of Mn substitution on the catalytic activity of spinel ferrite, all the catalysts were characterized in terms of microstructural environment and physicochemical properties.

3.3. Structure and surface characterization

3.3.1. Raman

The Raman spectra of spinel ferrite catalysts are shown in Fig. 3. The non-doped catalyst Mn0 shows four distinct bands at approximately 195 cm^{-1} (T_{2g}), 348 cm^{-1} (E_{1g}), 497 cm^{-1} (T_{2g}) and 693 cm^{-1} (A_{1g}), respectively, close to the active phonon modes of maghemite in the study by Graves et al. [48] and Chamritski et al. [49]. With the increase of Mn substitution, the peaks at low wavenumber gradually decrease in intensity, and some of them even disappear for Mn1.0. Moreover, the A_{1g} band gradually splits and finally shifts to low wavenumber. For example, the A_{1g} band is at 693 cm^{-1} for Mn0, but 642 cm^{-1} for Mn1.0. This would be ascribed to changes in dipole ordering by Mn introduction [50], illustrating the substitution of Mn for Fe. The Raman spectrum of Mn1.0 is consistent to that of spinel $MnFe_2O_4$ in the study by Graves et al. [48]. The Raman results indicate that all the catalysts are in the phase of spinel ferrite, which is in line with the observation in the XRD characterization.

3.3.2. TG-DSC

To investigate the changes of cation valence and catalyst phase during the formation of spinel ferrite, thermal analysis under air was carried out (Fig. 4). For the oxidation of Mn0 precursor, the DSC curve shows two main exothermic peaks. The former peak at ca. 157 °C is related to the oxidation of Fe^{2+} to form maghemite. In this stage, the mass gain is masked by the dehydroxylation process with obvious mass loss in the similar temperature range, which has been certificated by the TG-DSC analysis under nitrogen [51]. The latter peak at ca. 771 °C is ascribed to the phase transformation maghemite–hematite without mass changes. With the increase of
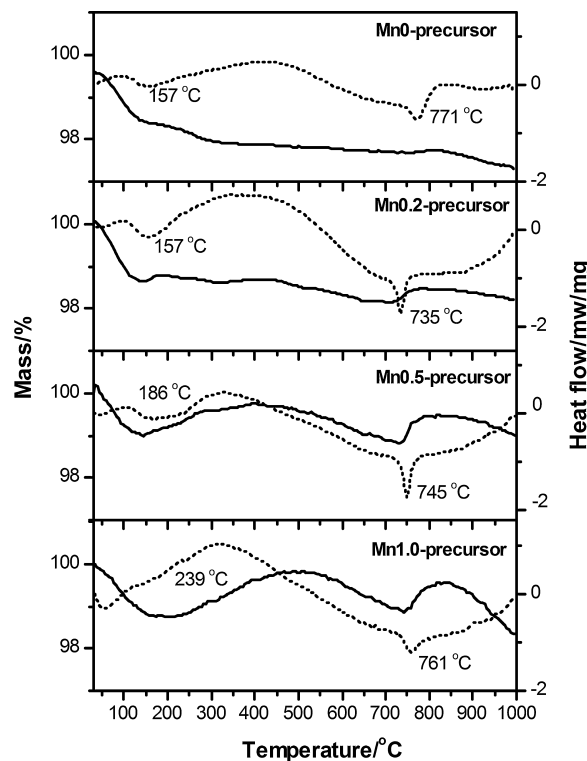
Mn^{2+} substitution in the precursor, the former exothermic peak gradually shifts to higher temperature, and the mass gain appears in the range of 150–450 °C, which is attributed to the oxidation of Fe^{2+}, Mn^{2+} and Mn^{3+} cations [52]. This indicates the higher oxidation temperature of Mn cation than Fe, due to the difference in the cation-oxygen distances. Different from the Mn0 precursor, the mass gain of Mn oxidation is not masked by the dehydroxylation process, because of the more oxygen uptake during the oxidation of Mn^{2+} to Mn^{4+} than Fe^{2+} oxidation. The mass gain is followed by a mass loss in the range of ca. 450–700 °C (Fig. 4), ascribed to the reduction of Mn^{4+} to Mn^{3+} or Mn^{2+}. Then another rapid mass gain is shown in the range of ca. 750–800 °C, where Mn^{2+} cations are finally oxidized to Mn^{3+} [52]. This further oxidation is followed by a lattice transformation from a spinel structure to hematite in which all the cations are trivalent. From the TG-DSC analysis, all the ferrite catalysts after calcination at 450 °C are in the main phase of maghemite and the spinel structure is still maintained, where the cations exist as Fe^{3+}, Mn^{3+} and Mn^{4+}.

3.3.3. XPS

To further confirm the oxidation states of the constituent elements on catalyst surface, XPS analysis was carried out with an emphasis on the peaks associated with Fe 2p, Mn 2p and O 1s (Fig. 5). The atomic ratio of the relative elements, calculated from the photoelectron peaks in Fig. 5, are summarized in Table 3.

Fig. 5a displays the XPS spectra in the Fe 2p region. The Fe 2p peaks are composed of two main asymmetric peaks, Fe $2p_{3/2}$ and Fe $2p_{1/2}$ with binding energies centered at about 711.0 and 725.0 eV, respectively, revealing that Fe^{3+} is the only oxidation state present on catalyst surface. For Fe $2p_{3/2}$ peaks, two contributions at about 710.2 ± 0.1 and 711.3 ± 0.4 eV are attributed to the Fe^{3+} cations with different occupancies in the spinel structure [53]. Another weak contribution with higher binding energy at 712.8 ± 0.5 eV, is assigned to Fe^{3+} bonded with hydroxyl groups [54].

Two broad and asymmetric peaks located around 642.0 and 653.3 eV (Fig. 5b) correspond to Mn $2p_{3/2}$ and Mn $2p_{1/2}$, respec-
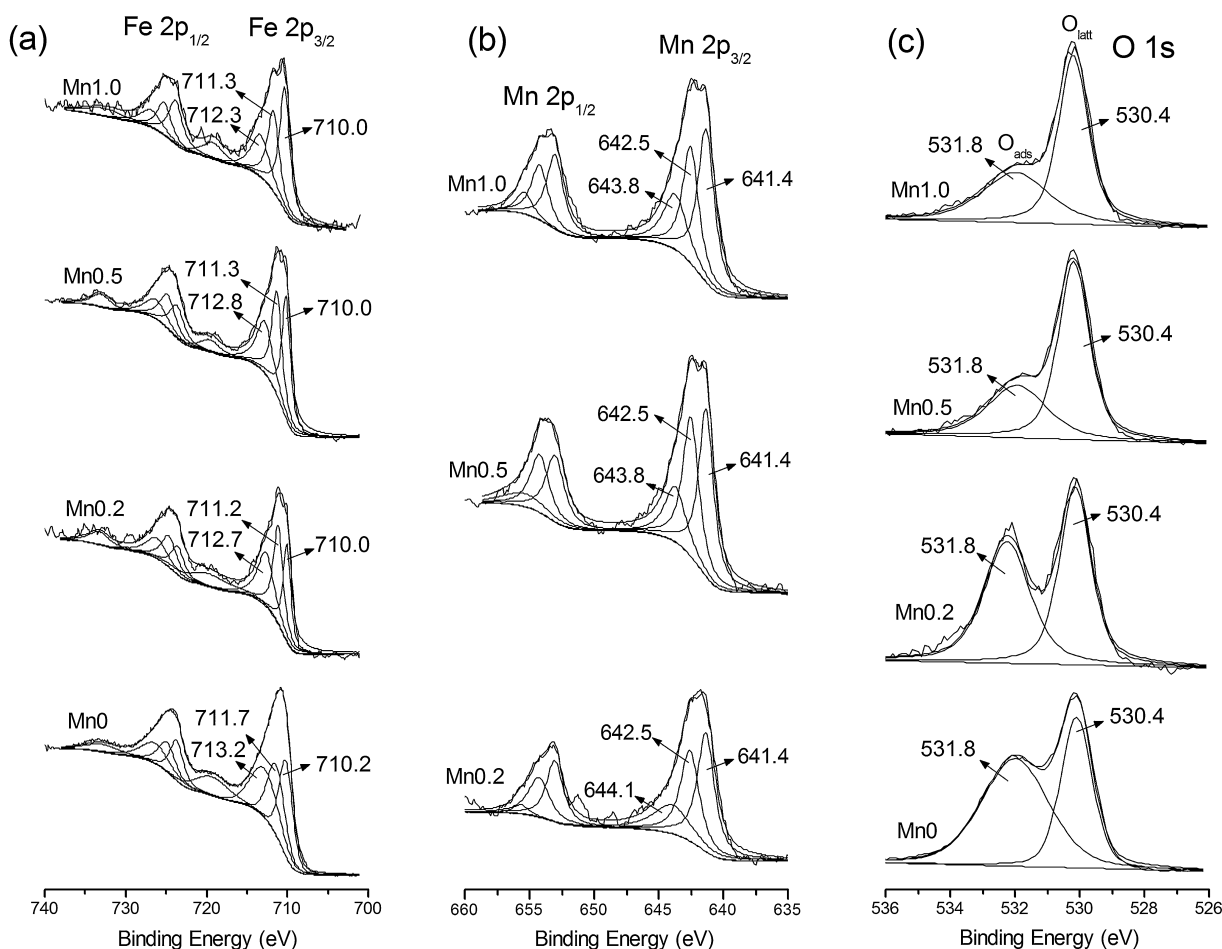
Fig. 5. XPS analysis of Mn doped ferrite catalysts: fitted Fe $2p_{1/2}$ and Fe $2p_{3/2}$ photoelectron peaks (a); fitted Mn $2p_{1/2}$ and Mn $2p_{3/2}$ photoelectron peaks (b); fitted O 1s photoelectron peaks (c).

Table 3
XPS relative intensity and bulk cationic distribution of the Mn substituted spinel ferrite.

Relative intensity	Mn0	Mn0.2	Mn0.5	Mn1.0
Mn^{3+} (% in intensity)	–	54.9	53.2	57.3
Mn^{4+} (% in intensity)	–	45.1	46.8	42.7
Mn^{3+}/Mn^{4+} (mole)	–	1.22	1.14	1.34
O_{latt} (% in intensity)	39.7	49.8	63.9	60.0
O_{ads} (% in intensity)	60.3	50.2	36.1	40.0
O_{latt}/O_{ads} (mole)	0.66	0.99	1.77	1.50
Mn (% in mole)	0	4.1	9.3	13.2
Fe (% in mole)	20.0	16.6	17.1	12.3
O (% in mole)	80.0	79.4	73.7	74.5
Mn/Fe (mole)	0	0.24	0.54	1.07
O/(Mn + Fe)	4.0	3.84	2.79	2.92

tively, separated by about 11.3 eV, in agreement with previous XPS spectra of Mn 2p reported by Tian et al. [55]. The Mn $2p_{3/2}$ can be deconvoluted into three contributions centered at 641.3 ± 0.1, 642.5 ± 0.1, and 643.9 ± 0.2 eV, attributed to Mn^{3+}, Mn^{4+} and Mn cations bonded with hydroxyl groups, respectively [56]. The Mn 2p peaks do not show a satellite feature at about 647 eV, which is characterized by MnO but not present for either Mn_2O_3 or MnO_2. This indicates the main valences of +3 and +4 for Mn cations on the ferrite surface. The XPS results for the valences of Mn and Fe cations are consistent to the observation from TG-DSC results. For all the catalysts with Mn substitution, the ratios of Mn^{3+}/Mn^{4+} on the surface are in the range of 1.14–1.34.

Fig. S1 displays the Mn 3s and Fe 3s spectra of Mn substituted spinel ferrites. The peak at 93.6 ± 0.1 eV is ascribed to the Fe 3s, whose intensity decreases with the increase of Mn content in ferrites. The Mn 3s peak has two main spilt components at 89.0 ± 0.2 and 83.4 ± 0.2 eV, caused by coupling of non-ionized 3s electron with 3d valence-band electrons. The magnitude of Mn 3s peak splitting (ΔE) is diagnostic of oxidation state. The ΔE for MnO, Mn_2O_3 and MnO_2 is 6.0, 5.5 and 4.7 eV. For Mn0.2, Mn0.5 and Mn1.0, the ΔE for Mn 3s peak is 5.7, 5.6 and 5.5 eV, indicating the average valency of Mn is close to +3. Compared to the Mn 2p XPS and TG-DSC results, the ΔE of Mn 3s suggests the lower valence of Mn cations in ferrites. From previous studies [57,58], the presence of foreign cations in manganese oxides reduces the degree of Mn-O covalency and accordingly increases the Mn 3s splitting. Therefore, the decrease of ΔE in this study is probably related to the presence of structural Fe cations. With the increase of Mn content, ΔE does not vary obviously. This indicates the similar Mn^{3+}/Mn^{4+} ratio in all the Mn substituted ferrite catalysts.

The asymmetric O 1s peaks with two-band structure are observed in Fig. 5c for all the samples. The O 1s peaks can be deconvoluted into two contributions at 530.4 and 531.8 eV, which are contributed to the lattice oxygen (O_{latt}) and surface adsorbed oxygen (O_{ads}), e.g., surface oxygen of hydroxyl species or adsorbed water species, respectively [59]. With Mn doping, the O_{latt}/O_{ads} ratio increases from 0.66 for the non-doped sample to 1.77 for the sample Mn0.5, and then does not change obviously in the sample Mn1.0.
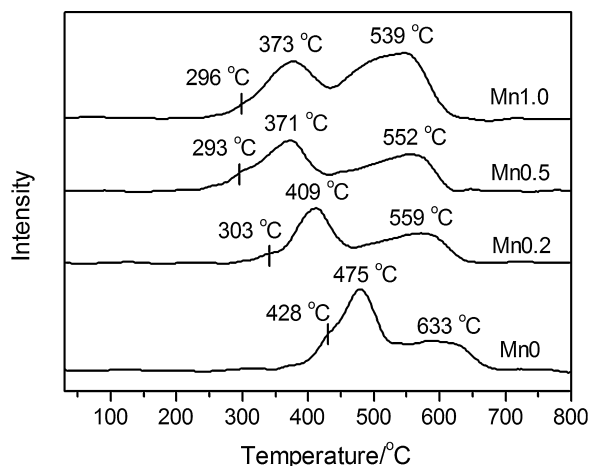
Fig. 6. The TPR profiles of the Mn substituted spinel ferrite catalysts.

Fig. 7. The relationship between the reduction temperature of bulk phase ferrite and the oxidation temperature T50 or T90.

To study the chemical heterogeneity, the chemical composition on the catalyst surface is compared to that in the bulk phase. The former composition on the surface was obtained from XPS analysis (Table 3), while the latter one was derived from chemical analysis. The surface Mn/Fe mole ratio for Mn0.2 is 0.24, obviously larger than that in the bulk structure (0.063, Table 1). This phenomenon becomes more obvious, as the Mn substitution increases. This indicates the Mn enrichment on the catalyst surface. The similar phenomenon has been observed in nanosized Mn substituted magnetite, where Mn distribution on magnetite surface increases with the increase of Mn content [60,61]. Moreover, the surface concentration of oxygen (Table 3) is considerably higher than the bulk phase for all the catalysts (Table 1), showing that the surface is more oxidized than the bulk. But surface concentration of oxygen decreases with the Mn substitution increase, further confirming the decrease of surface oxygen.

3.3.4. TPR

The TPR characterization was performed in order to obtain information about reducibility of catalysts (Fig. 6). For non-doped catalyst Mn0, its TPR profiles show mainly three sets of reduction processes. A small and weak reduction peak in the temperature range of ca. 400–450 °C can be observed for non-doped catalyst, which are associated with the reactive Fe^{3+} surface species [39]. A second reduction peak appears in the temperature range of ca. 450–520 °C, related to the reduction of bulk phase of ferrite to produce FeO phase. Then the FeO is completely reduced to metallic Fe, with reduction peak at ca. 633 °C. For catalysts with Mn substitution, the reduction peak related to Fe^{3+} reduction decreases in intensity, ascribed to the substitution of Fe^{3+} by Mn^{3+} or Mn^{4+}. Moreover, the reduction peak related to FeO reduction increases in intensity, due to the overlap of Mn^{3+} and Mn^{4+} reduction to MnO [62]. Another important feature observed in the TPR profiles is a shift of three reduction peaks to lower temperature as Mn is introduced in the spinel structure. This suggests that the presence of Mn facilitates the reduction of ferrite and enhances the oxidative ability of Fe^{3+} and Mn cations on the catalyst, which may be ascribed to the strong interaction between Fe^{3+} and Mn cations.

3.4. Structure-reactivity relationship

XRD and Raman results show that all the catalysts are with the spinel structure. The thermal analysis and XPS characterization results suggest that the cations exist as Fe^{3+}, Mn^{3+} and Mn^{4+}. From the shift activity results, it is observed that Mn substitution in spinel ferrite improves its catalytic activity for HCHO oxidation.
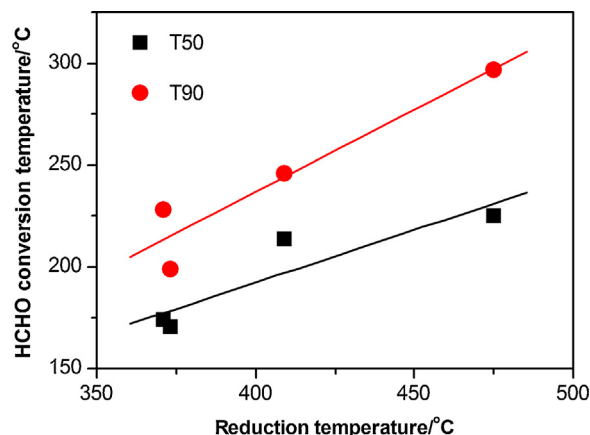
In previous studies, Mars-Van Krevelen (MVK) mechanism has been widely used for the catalytic oxidation of VOCs over metal oxides. The MVK mechanism involves the reaction between VOC molecule and oxygen on different redox sites of catalyst surface [43,63]. The reaction includes two-stage redox steps, i.e., oxidation of the catalyst by oxygen from the gas phase to form surface oxygen, which reacts with the VOCs molecules in the air, and reduction of the oxidized catalyst by hydrocarbon. Specifically for HCHO, its oxidation over metal oxide includes the reaction between HCHO and surface oxygen to form the intermediate formate (Eqs. (5) and (6)), and the oxidation of formate to H_2O and CO_2 by surface oxygen at different sites, accompanied with the catalyst reduced (Eqs. (7) and (8)) [33].

$$HCHO(g) + O(a) \rightarrow HCHOO(a) \qquad (5)$$

$$HCHOO(a) \rightarrow HCOO(a) + H(a) \qquad (6)$$

$$HCOO(a) \rightarrow H(a) + CO_2(g) \qquad (7)$$

$$2H(a) + O(a) \rightarrow H_2O \qquad (8)$$

where (g) and (a) refer to the gaseous and adsorbed species, respectively. Therefore, the overall activity of catalyst in HCHO oxidation depends on several parameters, e.g., the surface physico-chemistry properties of catalyst including specific surface area [64] and active site density that is related to the adsorption of oxygen and HCHO, and the reducibility of catalyst that is related to the release of oxygen to react with adsorbed hydrogen. In this study, the Mn substitution somewhat decreases the specific surface area (Table 1), and obviously decreases the surface oxygen content (Table 3), both of which would decrease the adsorption of HCHO on catalyst surface and slow its oxidation. Therefore, the improvement of catalytic activity for HCHO oxidation should rely on the increase of catalyst reducibility. From the TPR characterization, Mn substitution facilitates the reduction of spinel ferrite and improves the oxidative ability of metal cations on the catalyst surface for the oxidation of formate intermediate. A linear relationship between the reduction temperature of bulk phase ferrite and the oxidation temperature T50 (Table 2, $R^2 > 0.83$) or T90 (Table 2, $R^2 > 0.91$) can be observed (Fig. 7). At higher reaction temperature, for Mn1.0 with higher Mn substitution, more surface Mn^{3+} and Mn^{4+} was reduced than Mn0.5, resulted in the acceleration of electron transfer and phase reduction, and accordingly higher HCHO oxidation rate, which can explain the lower T90 of Mn1.0 than Mn0.5. This further confirms the main contribution of reducibility enhancement by Mn substitution on the improvement of catalytic activity for HCHO oxidation.
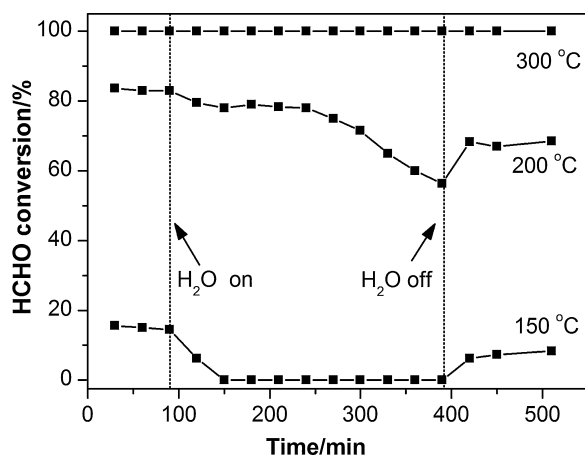
Fig. 8. Effect of moisture on HCHO conversion over the Mn0.5 catalyst at 150, 200 and 300 °C.
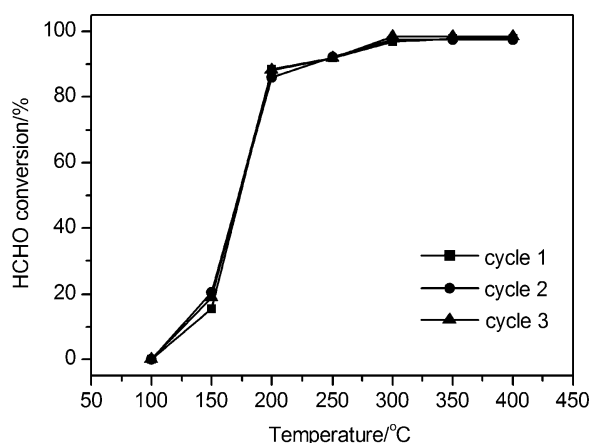

Fig. 9. The catalytic oxidation of HCHO over Mn0.5 in three cycles.

3.5. Moisture effect and catalytic stability

As is well known, moisture is one of major causes of the dramatic loss of catalytic activity, especially at low temperature [65]. Water adsorbed on the catalyst is known to adsorb both associatively and dissociatively (as −OH) on reduced cations and oxidize the surface, which blocks the unsaturated coordination sites on the catalyst surface and suppresses its catalytic activity [66]. In this study, we also compared the catalytic activity of Mn substituted spinel ferrite in the presence or absence of water vapor content ($5000\,mL\,m^{-3}$) in the HCHO/air stream. Mn0.5 was selected as the catalyst for moisture effect test at 150, 200 and 300 °C (Fig. 8). At 150 °C, the addition of water vapor decreased the HCHO conversion from 18% to zero, indicating the obvious deactivation effect of moisture at 150 °C. At 200 °C, after the introduction of water vapor, the conversion effect slowly decreased from 80% to 55%. However, at both 150 and 200 °C, the conversion rate was immediately increased after the moisture introduction stopped. Moreover, at 300 °C the addition of water did not cause apparent decrease in HCHO conversion. This may suggest that the Mn substituted spinel ferrite is catalytically durable in the studied temperature, and not sensitive to the presence of moisture at high temperature, e.g., 300 °C, unlike previously reported noble metal catalysts [15,16].

Besides the resistance to water, the stability of Mn doped ferrite catalyst is also critical for its applications. The life test was carried out by recycle experiment catalyzed by Mn0.5 catalyst. From Fig. 9, it can be found that the catalytic activity of Mn0.5 remained very stable in three cycles. In the 1st, 2nd and 3th cycles, T50 are all ca.

174 °C while T90 are 228, 234 and 231 °C, respectively. This indicates that the Mn substituted ferrite catalyst has a good long-term stability and activity. The catalyst has high stability and a superior activity in the presence of water vapor which presents an applied interest.

4. Conclusions

In the present study, Mn-doped spinel ferrite catalysts were synthesized by the activation of their magnetite precursors in air at 450 °C. The HCHO oxidation over these catalysts was tested. The catalysts are with spinel structure and Mn substitution does not change the crystal structure. Mn cations are in the valency of +3 and +4, enriching on the surface. The Mn substitution decreases the specific surface area and adsorbed oxygen content on the catalyst surface, both of which would decrease the HCHO adsorption on ferrite surface. Mn substitution obviously improves the catalytic activity of spinel ferrite for HCHO oxidation. TPR characterization results indicate Mn introduction facilitates the reduction of spinel ferrite and improve the oxidative ability of metal cations on the catalyst surface, which can explain the positive effect of Mn substitution on the catalytic activity for HCHO oxidation. The catalyst displays high stability and a superior activity in the presence of water vapor, which is benefit for its application.

Appendix A. Supplementary data

Supplementary data associated with this article can be found, in the online version, at http://dx.doi.org/10.1016/j.apcatb.2015.09.055.

References

[1] X.J. Tang, Y. Bai, A. Duong, M.T. Smith, L.Y. Li, L.P. Zhang, Environ. Int. 35 (2009) 1210–1224.
[2] O.J. Prado, M.C. Veiga, C. Kennes, Chemosphere 70 (2008) 1357–1365.
[3] C.T. Chang, K.L. Lin, Resourc. Conserv. Recycl. 46 (2006) 321–334.
[4] X.B. Zhu, X. Gao, R. Qin, Y.X. Zeng, R.Y. Qu, C.H. Zheng, X. Tu, Appl. Catal. B: Environ. 170 (2015) 293–300.
[5] Y. Huang, M.F. Han, J. Hazard. Mater. 193 (2011) 90–94.
[6] M. Chidambaram, S. Selvakumar, A.P. Singh, J. Mol. Catal. A: Chem. 245 (2006) 69–77.
[7] D. Kibanova, M. Sleiman, J. Cervini-Silva, H. Destaillats, J. Hazard. Mater. 211 (2012) 233–239.
[8] Z.P. Qu, D. Chen, Y.H. Sun, Y. Wang, Appl. Catal. A: Gen. 487 (2014) 100–109.
[9] W.X. Tang, X.F. Wu, S.D. Li, W.H. Li, Y.F. Chen, Catal. Commun. 56 (2014) 134–138.
[10] C.B. Zhang, Y.B. Li, Y.F. Wang, H. He, Environ. Sci. Technol. 48 (2014) 5816–5822.
[11] N.H. An, P. Wu, S.Y. Li, M.J. Jia, W.X. Zhang, Appl. Surf. Sci. 285 (2013) 805–809.
[12] B.C. Liu, C.Y. Li, Y.F. Zhang, Y. Liu, W.T. Hu, Q. Wang, L. Han, J. Zhang, Appl. Catal. B: Environ. 111 (2012) 467–475.
[13] Z.Y. Jin, P.P. Li, G.Y. Liu, B.Z. Zheng, H.Y. Yuan, D. Xiao, J. Mater. Chem. A 1 (2013) 14736–14743.
[14] C. Shi, Y. Wang, A.M. Zhu, B.B. Chen, C. Au, Catal. Commun. 28 (2012) 18–22.
[15] F.J. Varela-Gandia, A. Berenguer-Murcia, D. Lozano-Castello, D. Cazorla-Amoros, D.R. Sellick, S.H. Taylor, Appl. Catal. B: Environ. 129 (2013) 98–105.
[16] J.L. Lu, B.S. Fu, M.C. Kung, G.M. Xiao, J.W. Elam, H.H. Kung, P.C. Stair, Science 335 (2012) 1205–1208.
[17] W.B. Li, J.X. Wang, H. Gong, Catal. Today 148 (2009) 81–87.

[18] Y.S. Xia, H.X. Dai, L. Zhang, J.G. Deng, H. He, C.T. Au, Appl. Catal. B: Environ. 100 (2010) 229–237.
[19] L. Bai, F. Wyrwalski, J.F. Lamonier, A.Y. Khodakov, E. Monflier, A. Ponchel, Appl. Catal. B: Environ. 138 (2013) 381–390.
[20] M.R. Morales, B.P. Barbero, L.E. Cadus, Appl. Catal. B: Environ. 67 (2006) 229–236.
[21] C.Y. Ma, D.H. Wang, W.J. Xue, B.J. Dou, H.L. Wang, Z.P. Hao, Environ. Sci. Technol. 45 (2011) 3628–3634.
[22] M.R. Morales, B.P. Barbero, L.E. Cadus, Appl. Catal. B: Environ. 74 (2007) 1–10.
[23] F.Y. Cheng, J.A. Shen, B. Peng, Y.D. Pan, Z.L. Tao, J. Chen, Nat. Chem. 3 (2011) 79–84.
[24] A. Sutka, G. Mezinskis, A. Lusis, D. Jakovlevs, Sens. Actuat. B: Chem. 171 (2012) 204–209.
[25] F.G. Duran, B.P. Barbero, L.E. Cadus, C. Rojas, M.A. Centeno, J.A. Odriozola, Appl. Catal. B: Environ. 92 (2009) 194–201.
[26] F. Meshkani, M. Rezaei, Renew. Energy 74 (2015) 588–598.
[27] A. Khan, P. Chen, P. Boolchand, P.G. Smirniotis, J. Catal. 253 (2008) 91–104.
[28] Y.J. Tu, C.K. Chang, C.F. You, J. Hazard. Mater. 229 (2012) 258–264.
[29] S. Sun, X.Y. Yang, Y. Zhang, F. Zhang, J.J. Ding, J. Bao, C. Gao, Progr. Nat. Sci. Mater. Int. 22 (2012) 640–644.
[30] Y. Hammiche-Bellal, A. Benadda, L. Meddour-Boukhobza, S. Barama, A. Djadoun, A. Barama, Catal. Commun. 42 (2013) 62–67.
[31] G.K. Reddy, K. Gunasekara, P. Boolchand, P.G. Smirniotis, J. Phys. Chem. C 115 (2011) 920–930.
[32] T. Cai, H. Huang, W. Deng, Q.G. Dai, W. Liu, X.Y. Wang, Appl. Catal. B: Environ. 166 (2015) 393–405.
[33] Y. Sekine, Atmos. Environ. 36 (2002) 5543–5547.
[34] J.H. Zhang, Y.B. Li, L. Wang, C.B. Zhang, H. He, Catal. Sci. Technol. 5 (2015) 2305–2313.
[35] H. Tian, J.H. He, X.D. Zhang, L. Zhou, D.H. Wang, Microporous Mesoporous Mater. 138 (2011) 118–122.
[36] L. Zhou, J.H. He, J. Zhang, Z.C. He, Y.C. Hu, C.B. Zhang, H. He, J. Phys. Chem. C 115 (2011) 16873–16878.
[37] J. Papavasiliou, G. Avgouropoulos, T. Ioannides, J. Catal. 251 (2007) 7–20.
[38] A.G. Anshits, E.N. Voskresenskaya, E.V. Kondratenko, E.V. Fomenko, E.V. Sokol, Catal. Today 42 (1998) 197–203.
[39] L.C.A. Oliveira, J.D. Fabris, R.R.V.A. Rios, W.N. Mussel, R.M. Lago, Appl. Catal. A: Gen. 259 (2004) 253–259.
[40] B. Antic, A. Kremenovic, N. Jovic, M.B. Pavlovic, C. Jovalekic, A.S. Nikolic, G.F. Goya, C. Weidenthaler, J. Appl. Phys. 111 (2012), 074309.
[41] S.J. Yang, N.Q. Yan, Y.F. Guo, D.Q. Wu, H.P. He, Z. Qu, J.F. Li, Q. Zhou, J.P. Jia, Environ. Sci. Technol. 45 (2011) 1540–1546.
[42] W.W. Zhao, C.T. Li, P. Lu, Q.B. Wen, Y.P. Zhao, X. Zhang, C.Z. Fan, S.S. Tao, Environ. Technol. 34 (2013) 81–90.
[43] J.J. Pei, J.S.S. Zhang, Hvac&R Res. 17 (2011) 476–503.
[44] R.H. Wang, J.H. Li, Catal. Lett. 131 (2009) 500–505.
[45] Y.C. Hong, K.Q. Sun, K.H. Han, G. Liu, B.Q. Xu, Catal. Today 158 (2010) 415–422.
[46] S.J. Yang, C.Z. Wang, J.H. Li, N.Q. Yan, L. Ma, H.Z. Chang, Appl. Catal. B: Environ. 110 (2011) 71–80.
[47] G.Y. Popova, T.V. Andrushkevich, E.V. Semionova, Y.A. Chesalov, L.S. Dovlitova, V.A. Rogov, V.N. Parmon, J. Mol. Catal. A: Chem. 283 (2008) 146–152.
[48] P.R. Graves, C. Johnston, J.J. Campaniello, Mater. Res. Bull. 23 (1988) 1651–1660.
[49] I. Chamritski, G. Burns, J. Phys. Chem. B 109 (2005) 4965–4968.
[50] N.V. Sidorov, P.G. Chufyrev, M.N. Palatnikov, N.N. Mel'nik, V.T. Kalinnikov, Inorg. Mater. 41 (2005) 164–171.
[51] X.L. Liang, S.Y. Zhu, Y.H. Zhong, J.X. Zhu, P. Yuan, H.P. He, J. Zhang, Appl. Catal. B: Environ. 97 (2010) 151–159.
[52] B. Gillot, M. Laarj, S. Kacim, J. Mater. Chem. 7 (1997) 827–831.
[53] S.J. Yang, Y.F. Guo, N.Q. Yan, D.Q. Wu, H.P. He, Z. Qu, J.P. Jia, Ind. Eng. Chem. Res. 50 (2011) 9650–9656.
[54] C.L. Corkhill, P.L. Wincott, J.R. Lloyd, D.J. Vaughan, Geochim. Cosmochim. Acta 72 (2008) 5616–5633.
[55] Z.Y. Tian, P.H.T. Ngamou, V. Vannier, K. Kohse-Hoinghaus, N. Bahlawane, Appl. Catal. B: Environ. 117 (2012) 125–134.
[56] M.C. Biesinger, B.P. Payne, A.P. Grosvenor, L.W.M. Lau, A.R. Gerson, R.S. Smart, Appl. Surf. Sci. 257 (2011) 2717–2730.
[57] V.R. Galakhov, M. Demeter, S. Bartkowski, M. Neumann, N.A. Ovechkina, E.Z. Kurmaev, N.I. Logachevskaya, Y.M. Mukovskii, J. Mitchell, D.L. Ederer, Phys. Rev. B 65 (2002), 113102.
[58] G.C. Allen, S.J. Harris, J.A. Jutson, J.M. Dyke, Appl. Surf. Sci. 37 (1989) 111–134.
[59] S.D. Li, H.S. Wang, W.M. Li, X.F. Wu, W.X. Tang, Y.F. Chen, Appl. Catal. B: Environ. 166 (2015) 260–269.
[60] X.L. Liang, Z.S. He, G.L. Wei, P. Liu, Y.H. Zhong, W. Tan, P.X. Du, J.X. Zhu, H.P. He, J. Zhang, J. Colloid Interface Sci. 426 (2014) 181–189.
[61] X.L. Liang, Z.S. He, W. Tan, P. Liu, J.X. Zhu, J. Zhang, H.P. He, Phys. Chem. Miner. 42 (2015) 373–383.
[62] S.C. Kim, W.G. Shim, Appl. Catal. B: Environ. 98 (2010) 180–185.
[63] H.J. Wu, L.D. Wang, J.Q. Zhang, Z.Y. Shen, J.H. Zhao, Catal. Commun. 12 (2011) 859–865.
[64] H.B. Huang, Y. Xu, Q.Y. Feng, D.Y.C. Leung, Catal. Sci. Technol. 5 (2015) 2649–2669.
[65] H.J. Joung, J.H. Kim, J.S. Oh, D.W. You, H.O. Park, K.W. Jung, Appl. Surf. Sci. 290 (2014) 267–273.
[66] D.W. Kwon, P.W. Seo, G.J. Kim, S.C. Hong, Appl. Catal. B: Environ. 163 (2015) 436–443.